

EUV magnetic-dipole lines from highly-charged high-Z ions with an open $3d$ shell

D. Osin, J.D. Gillaspy, J. Reader, and Yu. Ralchenko^a

National Institute of Standards and Technology, Gaithersburg, MD 20899-8422, USA

Received: date / Revised version: date

Abstract. The electron beam ion trap (EBIT) at the National Institute of Standards and Technology was used to produce highly-charged ions of hafnium, tantalum and gold with an open $3d$ shell. The extreme-ultraviolet (EUV) spectra from these ions were recorded with a flat-field grazing-incidence spectrometer in the wavelength range of 4.5 nm to 25 nm. A total of 133 new spectral lines, primarily due to magnetic-dipole transitions within the ground-state $3d^n$ configurations of the Co-like to K-like ions, were identified by comparing energy-dependent experimental spectra with a detailed collisional-radiative modeling of the EBIT plasma.

PACS. XX.XX.XX No PACS code given

1 Introduction

Accurate knowledge of structure and spectra of highly-charged ions (HCI) is of great importance for atomic physics, astrophysics, and other fields of research [1, 2]. During the last decade there was a surge in spectroscopic studies of HCI of heavy elements for fusion applications [3]. This effort is primarily motivated by the proposed use of tungsten as a plasma-facing material in the divertor region of the international reactor ITER [4]. Atoms of tungsten will be sputtered from the divertor plates and are expected to deeply penetrate the plasma core. The core temperatures on the order of 10-20 keV are not sufficient to completely ionize tungsten, and therefore the partially ionized atoms will strongly emit in the x-ray and extreme ultraviolet (EUV) ranges of spectra. Although this will result in undesirable radiative power losses, on the positive side, the measured radiation can be reliably used to diagnose such plasma properties as, for example, temperature and density. This potential application stimulated an extensive analysis of W spectra (see, e.g., [5] and references therein), which resulted in identification of a large number of new spectral lines and in the development of new techniques for diagnostics of very hot plasmas [6, 7, 8].

The spectroscopic properties of other high-Z elements ($Z \sim 70 - 80$) are also a subject of active research. The interest in high-Z emission is not limited to the isoelectronic analysis of spectra with a goal of a better understanding of W emission. Since gold is one of the primary materials for hohlraums used in the inertial confinement fusion experiments [9], its highly-charged ions were studied in electron beam ion traps (EBITs) [6, 10, 11, 12], laser-produced plas-

mas [13, 14, 15, 16, 17], and tokamaks [18, 19, 20, 21]. Also, the alloys containing tantalum are considered to be another potential candidate for a plasma-facing material in tokamaks, and therefore the physical properties of Ta under the influence of hot plasmas are being examined too [22]. Our group has recently reported analysis of EUV spectra of Hf, Ta and Au from the EBIT at the National Institute of Standards and Technology (NIST) [23], where more than 100 new spectral lines from 35- to 52-times ionized atoms were identified. Those spectra are mainly due to the intrashell $n=4-n=4$ transitions in the ions with an open $4s$ or $4p$ shells.

Here we present measurements and identifications of EUV spectra from even higher (ion charge $z=44-60$) ions of Hf, Ta and Au with an open $3d$ shell in the ground configuration. The analogous spectra from tungsten ions were studied recently in Ref. [7], where we found that practically all spectral lines between 10 nm and 20 nm are due to the forbidden magnetic-dipole (M1) transitions within the ground state configurations $3d^n$. It was also found that many of the corresponding line ratios show high sensitivity to electron density in the range typical for fusion plasmas and thus can be used for diagnostics. In this work we continue application of the detailed collisional-radiative modeling to the analysis of spectral line intensities in EBIT plasmas and use it to identify the measured lines.

2 Experimental setup

The measurements of the EUV spectra of $3d^n$ ions of Hf, Ta and Au were carried out in the NIST EBIT, which produces an electron beam with a beam diameter of about $60 \mu\text{m}$ and a current density of about 3500 A cm^{-2} . The

^a e-mail: yuri.ralchenko@nist.gov

electron energy is controlled by applying a voltage to the central drift tube, and can be precisely varied in a range between 100 eV and 30 keV. The uncertainty in the electron beam energy is on the order of ± 50 eV, which is mainly caused by the space charge of the beam [24]. The design and operation principles of the EBIT are described in more detail elsewhere [25]. In these measurements, the electron beam energy was varied in a relatively narrow region between 4.0 keV and 6.5 keV for Hf and Ta, and 5.0 keV to 7.5 keV for Au (Table 1). This set of energies allowed us to produce spectra of all $3d^n$ ions of Hf, Ta and Au. The electron beam current was kept constant at 150 mA for all energies, the central drift tube potential was 220 V, and the ion loading duty cycle was 11 seconds throughout the entire set of measurements.

The metallic ions were introduced into the trap using the metal vapor vacuum arc ion source (MEVVA) [26]. Neutral gases, used mainly for wavelength calibration, were loaded into the trap through the gas injection system [27].

The spectral window observed in the course of these measurements extended from about 8 nm to 26 nm for Hf and Ta, and from 4.5 nm to 19.5 nm for Au. The spectra were recorded with a flat-field grazing-incidence EUV spectrometer, which is extensively described in [28]. The emitted radiation was collected from the 2-cm central region of the EBIT by a gold-coated spherical mirror, which focused the light onto the spectrometer entrance slit. The EUV spectrometer is equipped with a grazing incidence, aberration-corrected, variable-line-spacing grating, which has 1200 lines mm^{-1} in the center, and which produces a 2-D spectrally-dispersed image in a plane rather than on the Rowland circle [29], [30]. The vertical slit was kept wide-open in order to preserve a constant resolving power of about 400, as observed in [28], and in order to collect as much light as possible. The wide-open entrance slit, on the other hand, permits observation of the EBIT ion cloud shifts, which contribute to systematic error in the wavelength measurements. The spectra were recorded with a windowless nitrogen-cooled back-illuminated charge-coupled device (CCD) camera, which has a spectroscopic type chip with 1320×400 pixels of $20 \mu\text{m} \times 20 \mu\text{m}$ each. The total spectrum at every beam energy is combined from 20 one-minute spectra. This allows for easy removal of cosmic ray traces. In order to increase the signal-to-noise ratio, each individual spectral image is integrated over pixel columns aligned parallel to the image of the trapped ion cloud.

The measured spectra of Hf and Ta ions, observed in the region from 8 nm to 26 nm, were calibrated with known lines [31] of N^{3+} - N^{6+} , Kr^{17+} - Kr^{33+} , O^{4+} - O^{5+} , Fe^{16+} - Fe^{23+} , and Xe^{39+} - Xe^{43+} . For the Au spectra, calibration lines of Ar^{7+} - Ar^{8+} and Ne^{5+} - Ne^{7+} were used in addition to the O, Fe, and Xe lines. It should be mentioned that some calibration lines of highly ionized Xe were identified in our previous EBIT run [23] (see also [32]). Both the MEVVA and the gas injector were utilized to introduce the calibration elements into the EBIT trap. The calibration spectra were measured in a relatively broad range of

beam energies from 1250 eV to 9300 eV in order to cover the entire spectral range.

The calibration lines were fitted with statistically-weighted Gaussian line profiles. The calibration curve was obtained by the weighted fit of the line center positions determined in CCD pixels to the known wavelengths using a fourth-order polynomial. The weighting in the fit contained contributions from the Gaussian fit uncertainties, the uncertainty in the assigned calibration wavelengths, and the estimated systematic measurement uncertainty (a constant value in CCD pixels, which was converted into wavelength using the known dispersion of the spectrometer [28]). The quadrature sum of the three uncertainty components yielded the final uncertainty of the wavelength. The statistical uncertainties in line positions were typically less than 0.001 nm. Multiple wavelength values observed at different beam energies were weight averaged. The total error in the final wavelength was taken to be the quadrature sum of the total uncertainty from the calibration curve and the statistical uncertainty from the weighted average. The final uncertainty of the Hf, Ta and Au spectral lines was mainly on the order of 0.003 nm and somewhat higher for blended lines.

Figures 1-3 show the evolution of the measured spectra of Hf, Ta and Au with the beam energy. The signal counts in figures are the CCD analog-to-digital units (ADU). The high signal-to-noise ratio obtained in the spectra was important for identification of blended and weak spectral lines. The spectra contain a number of lines from impurity elements. The NIST EBIT is routinely used for various other studies including Xe deposition on surfaces, and therefore xenon lines are almost always seen in our spectra. For instance, several lines from the Xe ions with ion charge $z \approx 40$ are observed between 15 nm and 17 nm. Also, several lines from highly-charged O and Ar can be identified as well. In some cases the impurity lines blend with the lines from Hf, Ta and Au (e.g., Ar XV line at 22.115 nm with 22.091 nm line from Cr-like Hf). However, their contribution can be reliably isolated using the energy dependence of spectra and comparison with the simulated spectra which do not include impurities. Some of the impurity lines are indicated in Fig. 1.

3 Collisional-radiative modeling and line identifications

As with our previous studies [6,7,33,34,35], the spectral analysis and line identifications are based on detailed collisional-radiative (CR) modeling. In [7] we comprehensively described the basic principles of CR simulations for W ions with an open $3d$ shell, and the present simulations follow that approach. Briefly, we start with calculation of all required atomic data (energies, radiative probabilities and electron-impact cross sections) using the Flexible Atomic Code (FAC) [36]. The CR model includes singly-excited states up to at least $n=5$ (up to $n=8$ for ions near closed shells) as well as doubly-excited states with $n=3$. In order to reduce the number of states included, the $n \geq 4$

levels are combined into “superterms,” which were introduced in [7]; this results in more manageable matrix sizes without loss of accuracy. The energies of the singly- and doubly-excited states within $n=3$, which are the most important for the present study, are improved by performing additional extensive calculations which include all possible configurations of the $n = 3$ complex as well as the configurations described above. The calculated atomic data is then used as input to the non-Maxwellian CR code NO-MAD [37], which calculates ionization distributions (also taking into account charge exchange between ions and neutrals in the EBIT), level populations, and spectral line intensities. Finally, the theoretical spectrum is convolved with the spectrometer efficiency curve and compared with the measured spectra. This procedure allows us to identify the spectral lines using not only their wavelengths but also their line intensities.

The calculated ionization potentials for the Ni-like to Cl-like ions of Hf, Ta and Au are presented in Table 2. Also the Dirac-Fock results of Ref. [38] are given for comparison. The two sets of ionization energies are seen to agree within 0.4% or less. One can see then that the electron beam energies of Table 1 are sufficient to produce the required ionization stages with $3d^n$ ground configurations.

The experimental spectra in Figs. 1–3 cover a quite large range of wavelengths. This is achieved with a moderate spectral resolution $\lambda/\delta\lambda \sim 400$ that results in a number of blended lines. In such cases, the corresponding wavelengths were determined from those spectra where the abundance of one of the ions is small. This procedure is exemplified by the line at ~ 17.3 nm which was found to be very strong between 4350 eV and 5035 eV (Fig. 1). Closer inspection (see Fig. 4) shows that at lower values of the beam energy E_b , the main contribution comes from the 17.263 nm line in the Mn-like ion, while at higher energies only the 17.300 nm line in the Cr-like ion survives. Accordingly, the wavelengths of these two lines were derived from the spectra measured at the lowest or highest energies of the beam. Figure 1 also shows a strong line from Fe-like Hf⁴⁷⁺ at 17.424 nm that is blended with an impurity line at 17.438 nm. In order to analyze possible impurities, we routinely measured EBIT spectra without the metal ion injection. Such background spectra at approximately 5000 eV show a clear presence of an impurity at 17.438 nm; the wavelength of this line was derived from a Gaussian fit, and its contribution to the wide line profile with Hf injection was accounted for in a two-Gaussian fit.

Tables 3–5 present the measured wavelengths, line identifications, theoretical wavelengths and transition probabilities for 135 identified spectral lines, 133 of which are new. The identifications calculated by FAC are given in jj-coupling, and the notations used are described in [7]. For such highly-charged ions this type of coupling is the most appropriate. In the tables, l_{\pm} denotes an electron state with the total angular momentum $j=l \pm 1/2$, so that d_+ corresponds to $j=5/2$ and so on. Also, the wavelength uncertainties in the tables are given in the units of the last significant digit, so that 16.281(4) means 16.281 ± 0.004 .

3.1 Hf spectra

Table 3 presents 43 new spectral lines from Ni-like Hf⁴⁴⁺ to Ar-like Hf⁵⁴⁺. Except for the four M1 lines within the excited configurations $3p^5 3d^2$ of K-like and $3p^5 3d$ of Ar-like ions, almost all other lines correspond to the M1 transitions within the ground state configurations $3d^n$, $n=1-9$. The only non-M1 transition identified in the Hf spectra is the electric-quadrupole (E2) line at 16.149 nm in Ca-like Hf⁵²⁺, for which the M1 transition is not allowed by the $|\Delta J| \leq 1$ selection rule. The lowest-energy spectra in Fig. 1 also contain several lines from Cu-like and Ni-like ions which have been analyzed in our previous work [23]. In the present work the M1 transition within the excited configuration $3d^9 4s$ of Ni-like Hf⁴⁴⁺ was identified at 21.944 ± 0.003 nm; the recent result of 21.9377 nm from the relativistic many-body perturbation theory (RMBPT) [39] thus reasonably agrees with our value. The measured wavelength for the strong resonance line $4s-4p$ in the Cu-like ion is 13.372 ± 0.003 nm which excellently agrees both with our previous result of 13.373 ± 0.003 nm [23] and with the older tokamak measurement of 13.375 ± 0.005 nm [20].

The only two lines for which there exist theoretical wavelength calculations are the $3d_{5/2}^9-3d_{3/2}^9$ transition in the Co-like ion and the $3d_{3/2}-3d_{5/2}$ transition in the K-like ion. For the former, our measured wavelength of 21.229 ± 0.003 nm agrees within uncertainties with the semiempirical prediction of 21.202 ± 0.033 nm [40], while the calculated FAC value is slightly outside the experimental error bars. As also was the case for the W measurements [23], the measured wavelength of 18.158 ± 0.003 nm for the M1 line in K-like ion agrees very well with the multiconfiguration Dirac-Fock (MCDF) result of 18.1578 nm obtained by Ali and Kim [41].

The last column in Table 3 shows the calculated transition probabilities for the identified lines of Hf. The M1 lines have A values in the range of $8 \times 10^4 \text{ s}^{-1}$ to $3 \times 10^6 \text{ s}^{-1}$. The transition probability for the electric-quadrupole line at 16.149 nm is much smaller, about $2.8 \times 10^2 \text{ s}^{-1}$, which exemplifies relative weakness of intraconfiguration E2 lines as compared to M1 transitions.

3.2 Ta spectra

We identified 50 new lines from thirteen ions from Ni-like Ta⁴⁵⁺ to S-like Ta⁵⁷⁺ (Table 4). The identified lines correspond to intraconfiguration M1 transitions, although not all originate from the ground configurations: for instance, all lines in Ar-, Cl-, and S-like ions are within the $3p^n 3d$ configurations with $n=3-5$. Similar to the Hf case, the MCDF calculations of Ali and Kim agree very well with our wavelength for the $3d$ line in the K-like ion [41], and Safronova et al.’s RMBPT data [39] are very close to the measured wavelength in the Ni-like ion. The semiempirical value of 19.816 ± 0.032 nm for the M1 line in the Co-like ion agrees with our measured wavelength of 19.843 ± 0.003 nm within the stated uncertainties.

3.3 Au spectra

Forty new spectral lines were identified for ions of Au, from Ni-like Au⁵¹⁺ to K-like Au⁶⁰⁺ (Table 5). The higher ion charges for the isoelectronic ions of Au, as compared to Ta and Hf, result in smaller relative wavelength separations between the analogous spectral lines. Therefore, the lines overlap more often and are more difficult to analyze. This explains the relatively smaller number of identified lines for Au. Similar to the Hf and Ta cases, the RMBPT [39] and MCDF [41] results for Ni-like and K-like ions, respectively, agree well with the measured wavelengths, and again, the semiempirical wavelength for the $3d^9$ intraconfiguration transition in the Co-like ion agrees within uncertainties.

Two electric-quadrupole lines were identified in the measured spectra of Au. As mentioned above, the transition probabilities for E2 lines are typically much smaller than for M1 lines, and therefore they are more difficult to observe due to collisional damping. Indeed, our calculations show that the A-values for the E2 line at 11.993 nm in the V-like ion and for the E2 line in the Sc-like ion are only $7.97 \times 10^2 \text{ s}^{-1}$ and $1.55 \times 10^3 \text{ s}^{-1}$, respectively, while the A-values for M1 lines are on the order of 10^6 s^{-1} . The fact that such low-A lines were observed in the EBIT is due to their high branching ratios: both E2 transitions are the strongest for their corresponding upper levels.

We also identified two known lines in the Ni-like and Co-like ions of Au. The newly measured wavelengths of $13.858 \pm 0.003 \text{ nm}$ and $13.517 \pm 0.003 \text{ nm}$ agree within uncertainties with our previous results of $13.860 \pm 0.003 \text{ nm}$ and $13.522 \pm 0.003 \text{ nm}$ [23]. Thus, the recommended averaged values for these lines are $13.8590 \pm 0.0020 \text{ nm}$ for the $3d^9 4s$ transition in the Ni-like Au⁵¹⁺ and $13.5195 \pm 0.0020 \text{ nm}$ for the $3d^9$ transition in the Co-like Au⁵²⁺.

4 Conclusions

In this paper we presented measurements and identifications of a large number of EUV spectral lines originating from forbidden transitions, mostly within the ground configurations, in the $3d^n$ ions of Hf, Ta, and Au. These results provide a new accurate set of atomic data for highly-charged ions of high-Z elements which are important for magnetic and inertial confinement fusion research. Moreover, the measured wavelengths can also be used to test the most advanced theories of atomic structure in the relativistic regime.

As was shown in our previous work [7], the intensity ratios for similar M1 lines in the $3d^n$ ions of W are very sensitive to electron densities in the parameter range of magnetic fusion plasmas. Since the physical processes affecting level populations for Hf, Ta and Au are the same as those for W, one can expect similar sensitivity for the presently measured lines as well. The only minor difference will be that the sensitivity range of densities for Hf and Ta ions will be slightly shifted to lower densities while for Au it will be shifted to higher densities. This results from a strong z -dependence of the M1 radiative rates.

5 Acknowledgments

We are grateful to J. M. Pomeroy, J. N. Tan, and S. M. Brewer for assistance during the early experimental phase of this work, to U. I. Safronova for providing the energy levels of Ni-like ions from Ref. [39], and to Y.A. Podpaly for valuable comments. This work is supported in part by the Office of Fusion Energy Sciences of the U.S. Department of Energy.

References

1. H. Beyer, V. Shevelko, "Introduction to the Physics of the Highly Charged Ions", Series In Atomic And Molecular Physics (IOP Publishing Ltd, 2003)
2. J. Gillaspay, J. Phys. B: At. Mol. Opt. Phys **34**, R93 (2001)
3. R. Neu, K.B. Fournier, D. Bolshukhin, R. Dux, Phys. Scr. **T92**, 307 (2001)
4. R.J. Hawryluk, D. Campbell, G. Janeschitz, P. Thomas, R. Albanese, R. Ambrosino, C. Bachmann, L. Baylor, M. Becoulet, I. Benfatto et al., Nucl. Fusion **49**, 065012 (2009)
5. A. Kramida, Can. J. Phys. **89**, 551 (2011)
6. Yu. Ralchenko, I.N. Draganic, J.N. Tan, J.D. Gillaspay, J.M. Pomeroy, J. Reader, U. Feldman, G.E. Holland, J. Phys. B **41**, 021003 (2008)
7. Yu. Ralchenko, I.N. Draganic, D. Osin, J.D. Gillaspay, J. Reader, Phys. Rev. A **83**, 032517 (2011)
8. Yu. Ralchenko, J. Phys. B **40**, F175 (2007)
9. S.H. Glenzer, B.K. Spears, M.J. Edwards, E.T. Alger, R.L. Berger, D.L. Bleuel, D.K. Bradley, J.A. Caggiano, D.A. Callahan, C. Castro et al., Plasma Phys. Contr. Fusion **54**, 045013 (2012)
10. E. Träbert, J. Clementson, P. Beiersdorfer, J.A. Santana, Y. Ishikawa, Phys. Rev. A **82**, 062519 (2010)
11. S.B. Utter, P. Beiersdorfer, E. Träbert, Can. J. Phys. **81**, 911 (2003)
12. S.B. Utter, P. Beiersdorfer, E. Träbert, E.J. Clothiaux, Phys. Rev. A **67**, 032502 (2003)
13. J. Reader, G. Luther, Phys. Rev. Lett. **45**, 609 (1980)
14. J. Reader, G. Luther, Phys. Scr. **24**, 732 (1981)
15. J.F. Seely, J.O. Ekberg, C.M. Brown, U. Feldman, W.E. Behring, J. Reader, M.C. Richardson, Phys. Rev. Lett. **57**, 2924 (1986)
16. D.R. Kania, B.J. MacGowan, C.J. Keane, C.M. Brown, J.O. Ekberg, J.F. Seely, U. Feldman, J. Reader, J. Opt. Soc. Am. B **7**, 1993 (1990)
17. C.M. Brown, J.F. Seely, D.R. Kania, B.A. Hammel, C.A. Back, R.W. Lee, A. Bar-Shalom, W.E. Behring, At. Data Nucl. Data Tables **58**, 203 (1994)
18. J. Sugar, V. Kaufman, W.L. Rowan, J. Opt. Soc. Am. B **10**, 799 (1993)
19. H. Watanabe, D. Crosby, T. Fukami, D. Kato, S. Ohtani, J.D. Silver, C. Yamada, Phys. Rev. A **63**, 042513 (2001)
20. T. Pütterich, Ph.D. thesis, Universität Augsburg, IPP Garching, Germany (2006)
21. G.V. Brown, S.B. Hansen, E. Träbert, P. Beiersdorfer, K. Widmann, H. Chen, H.K. Chung, J.H.T. Clementson, M.F. Gu, D.B. Thorn, Phys. Rev. E **77**, 066406 (2008)
22. T. Hirai, M. Rubel, V. Philipps, A. Huber, T. Tanabe, M. Wada, T. Ohgo, A. Pospieszczyk, G. Sergienko, P. Wienhold, Phys. Scr. **T103**, 59 (2003)

23. I.N. Draganić, Yu. Ralchenko, J. Reader, J.D. Gillaspy, J.N. Tan, J.M. Pomeroy, S.M. Brewer, D. Osin, *J. Phys. B* **44**, 025001 (2011)
24. E. Takács, E.S. Meyer, J.D. Gillaspy, J.R. Roberts, C.T. Chantler, L.T. Hudson, R.D. Deslattes, C.M. Brown, J.M. Laming, U. Feldman et al., *Phys. Rev. A* **54**, 1342 (1996)
25. J.D. Gillaspy, *Phys. Scr.* **T71**, 99 (1997)
26. G.E. Holland, C.N. Boyer, J.F. Seely, J.N. Tan, J.M. Pomeroy, J.D. Gillaspy, *Rev. Sci. Instr.* **76**, 073304 (2005)
27. K. Fahy, E. Sokell, G. O'Sullivan, A. Aguilar, J.M. Pomeroy, J.N. Tan, J.D. Gillaspy, *Phys. Rev. A* **75**, 032520 (2007)
28. B. Blagojević, E.O. Le Bigot, K. Fahy, A. Aguilar, K. Makonyi, E. Takacs, J.N. Tan, J.M. Pomeroy, J.H. Burnett, J.D. Gillaspy et al., *Rev. Sci. Instrum.* **76**, 083102 (2005)
29. T. Harada, T. Kita, *Applied Optics* **19**, 3987 (1980)
30. T. Kita, *Applied Optics* **22**, 512 (1983)
31. Yu. Ralchenko, A. Kramida, J. Reader, and NIST ASD Team, NIST Atomic Spectra Database (ver. 4.1.0), [Online]. Available: <http://physics.nist.gov/asd> [2011, July 15]. National Institute of Standards and Technology, Gaithersburg, MD. (2011)
32. D. Osin, J. Reader, J.D. Gillaspy, Yu. Ralchenko, to be published (2012)
33. Yu. Ralchenko, J.N. Tan, J.D. Gillaspy, J.M. Pomeroy, E. Silver, *Phys. Rev. A* **74**, 042514 (2006)
34. Yu. Ralchenko, J. Reader, J.M. Pomeroy, J.N. Tan, J.D. Gillaspy, *J. Phys. B* **40**, 3861 (2007)
35. J.D. Gillaspy, I.N. Draganić, Yu. Ralchenko, J. Reader, J.N. Tan, J.M. Pomeroy, S.M. Brewer, *Phys. Rev. A* **80**, 010501 (2009)
36. M.F. Gu, *Can. J. Phys* **86**, 675 (2007)
37. Yu. Ralchenko, Y. Maron, *J. Quant. Spectr. Rad. Transf.* **71**, 609 (2001)
38. G.C. Rodrigues, P. Indelicato, J.P. Santos, P. Patté, F. Parente, *At. Data Nucl. Data Tables* **86**, 117 (2004)
39. U.I. Safronova, A.S. Safronova, P. Beiersdorfer, *J. Phys. B* **40**, 955 (2007)
40. J.O. Ekberg, U. Feldman, J.F. Seely, C.M. Brown, J. Reader, N. Acquista, *J. Opt. Soc. Am. B* **4**, 1913 (1987)
41. M.A. Ali, Y. Kim, *J. Opt. Soc. Am. B* **9**, 185 (1992)

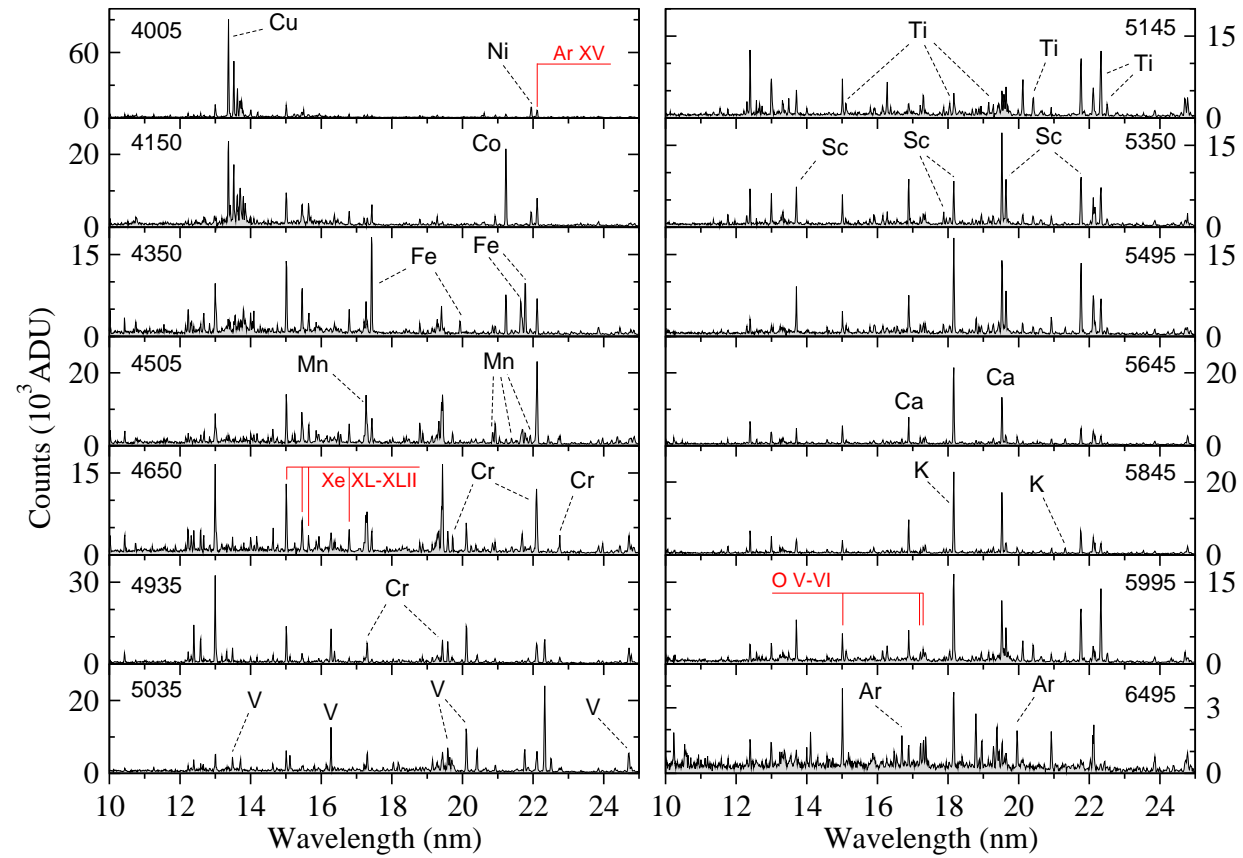


Fig. 1. Experimental spectra for Hf. Nominal beam energies (in eV) are shown in the upper corners. Some strong identified lines are indicated by their isoelectronic sequences. Several impurity lines from Xe and O are indicated as well.

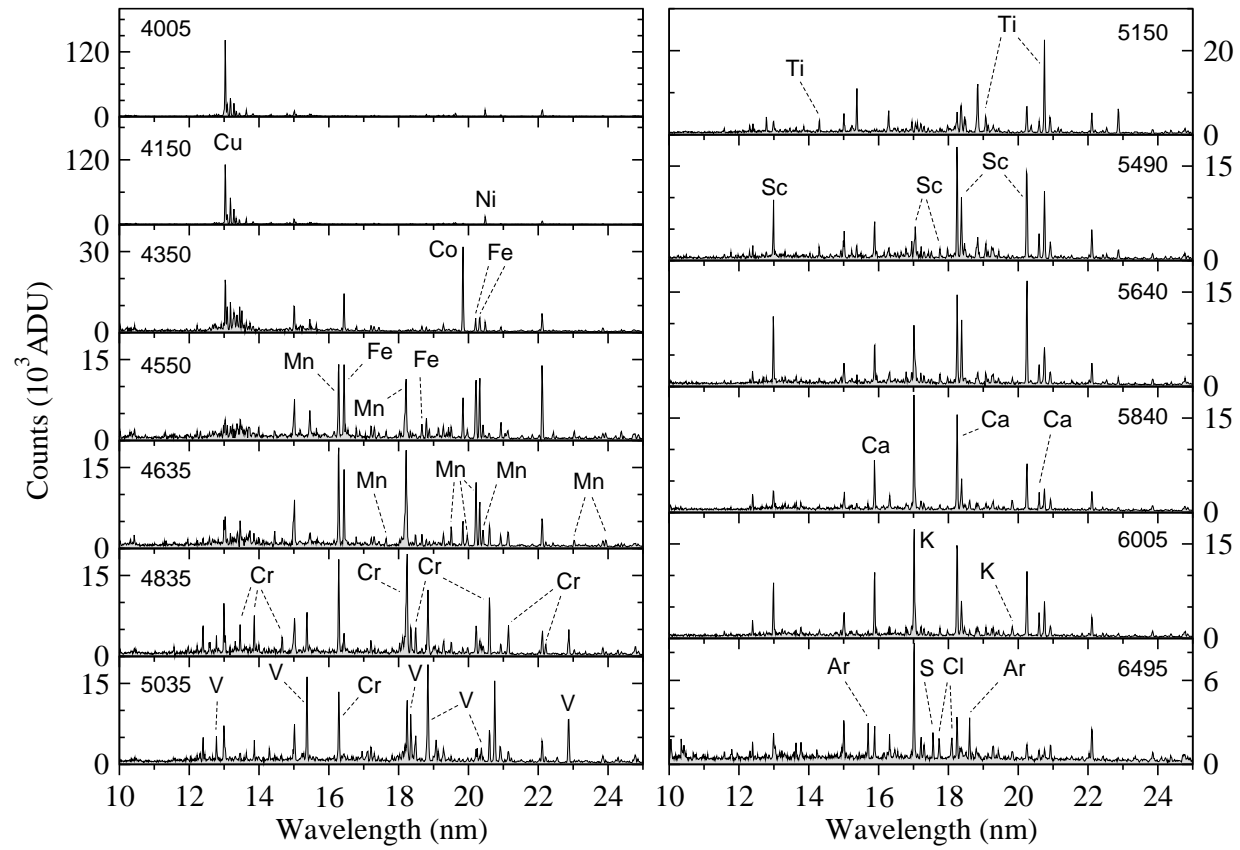


Fig. 2. Experimental spectra for Ta. Nominal beam energies (in eV) are shown in the upper corners. Some strong identified lines are indicated by their isoelectronic sequences.

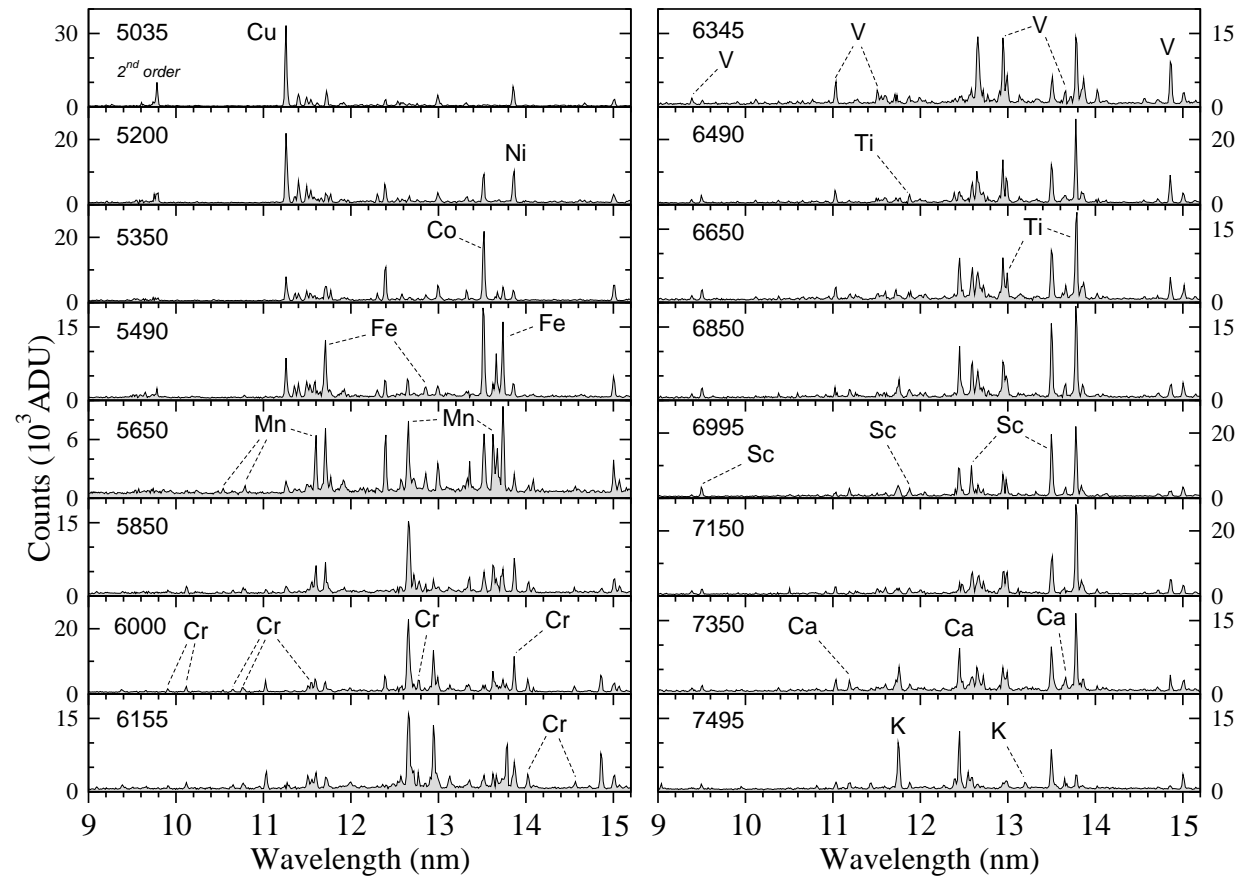


Fig. 3. Experimental spectra for Au. Nominal beam energies (in eV) are shown in the upper corners. Some strong identified lines are indicated by their isoelectronic sequences.

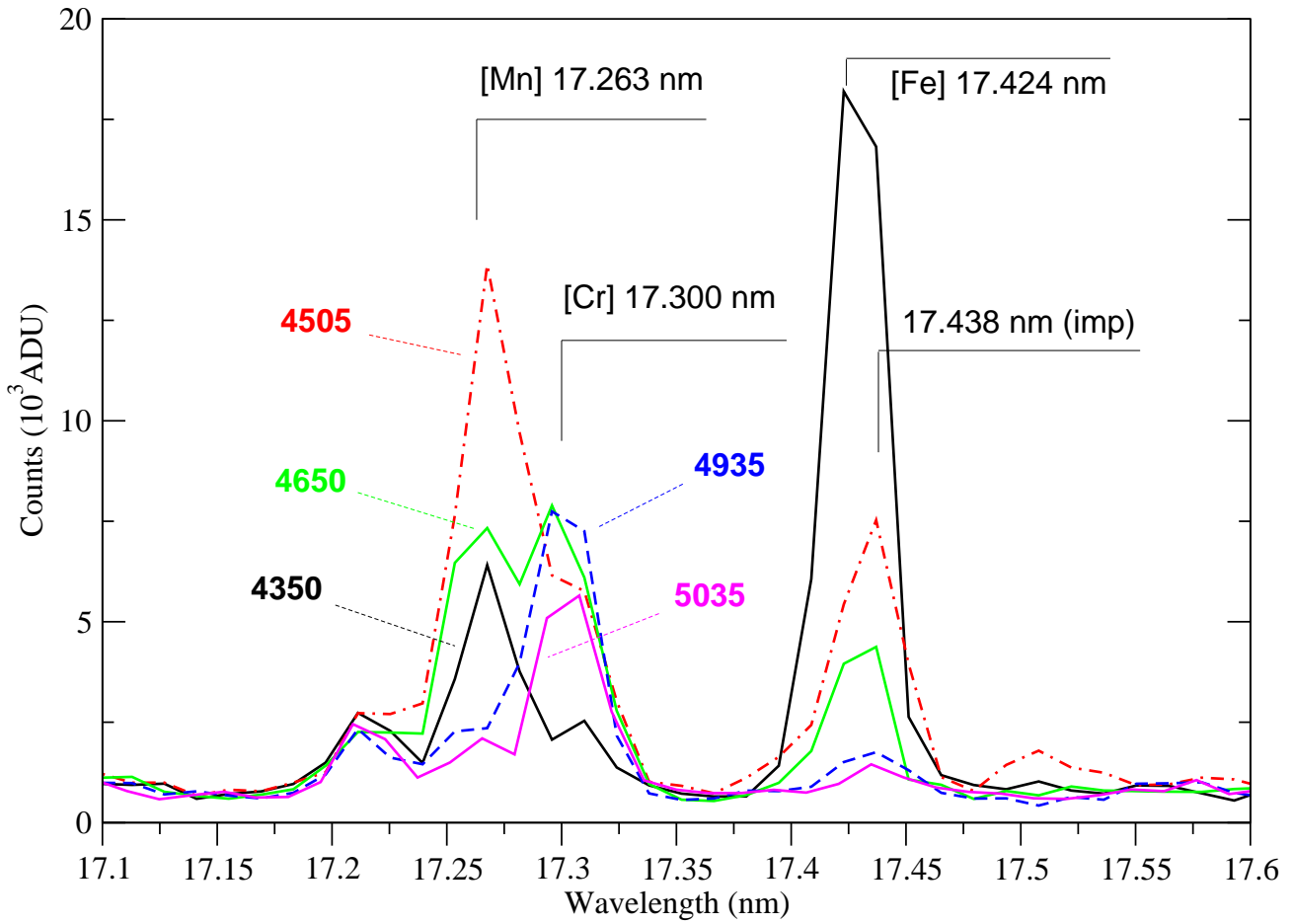


Fig. 4. Hafnium spectra near 17.3 nm at the nominal beam energies between 4350 eV and 5035 eV. The unknown impurity line at 17.438 nm was prominent in the background spectra.

Table 1. Nominal electron beam energies (in eV) used in the present work.

Hf	4005	4150	4350	4505	4650	4935	5035	5145	5350	5495	5645	5845	5995	6495
Ta	4005	4150	4350	4550	4635	4835	5035	5150	5490	5640	5840	6005	6495	
Au	5035	5200	5350	5490	5650	5850	6000	6155	6345	6490	6650	6850	6995	7150 7350 7495

Table 2. Calculated ionization potentials (in eV) of Ni-like through Cl-like ions of Hf, Ta and Au.

Sequence	Hf		Ta		Au	
	FAC	Ref. [38]	FAC	Ref. [38]	FAC	Ref. [38]
Ni $3d^{10}$	3741.7	3741	3895.3	3898.7	4880.4	4888
Co $3d^9$	3859.4	3858	4015.2	4014	5014.0	5013
Fe $3d^8$	3984.9	3984	4143.1	4143	5156.0	5156
Mn $3d^7$	4119.1	4118	4279.8	4278	5307.9	5307
Cr $3d^6$	4248.2	4246	4411.3	4410	5453.7	5452
V $3d^5$	4375.7	4372	4541.0	4537	5596.4	5594
Ti $3d^4$	4576.9	4573	4749.1	4745	5850.8	5846
Sc $3d^3$	4709.1	4703	4883.6	4877	5999.5	5994
Ca $3d^2$	4853.3	4846	5030.4	5024	6162.3	6156
K $3d$	4987.6	4980	5167.1	5159	6313.6	6305
Ar $3p^6$	5359.8	5350	5545.9	5537	6732.4	6724
Cl $3p^5$	5474.9	5468	5663.0	5655	6861.3	6854

Table 3. Identified spectral lines of highly-charged ions of hafnium. Level identifications include calculated level numbers. Blended lines are indicated by “b”. Notation a(b) for transition probabilities A means $a \cdot 10^b$. The electric-quadrupole line is marked by asterisk. Other theoretical works: A – [39], B – [40], C – [41].

Ion charge	Seq.	Conf.	Lower level		Upper level		λ_{exp} (nm)	λ_{th} (nm)	A (s ⁻¹)
			No.	Term _J	No.	Term _J			
44	Ni	3d ⁹ 4s	3	((d ₊ ⁵) _{5/2} , s ₊) ₂	4	((d ₋ ³) _{3/2} , s ₊) ₁	21.944(3)	22.0114, 21.9377 ^A	1.60(6)
45	Co	3d ⁹	1	(d ₊ ⁵) _{5/2}	2	(d ₋ ³) _{3/2}	21.229(3)	21.3176, 21.202(33) ^B	1.65(6)
46	Fe	3d ⁸	1	(d ₊ ⁴) ₄	7	((d ₋ ³) _{3/2} , (d ₊ ⁵) _{5/2}) ₄	17.424(8)	17.3934	6.90(5)
46	Fe	3d ⁸	2	(d ₊ ⁴) ₂	6	((d ₋ ³) _{3/2} , (d ₊ ⁵) _{5/2}) ₁	19.929(3)	19.9516	1.15(6)
46	Fe	3d ⁸	2	(d ₊ ⁴) ₂	5	((d ₋ ³) _{3/2} , (d ₊ ⁵) _{5/2}) ₂	21.652(5)	21.7390	1.29(6)
46	Fe	3d ⁸	1	(d ₊ ⁴) ₄	4	((d ₋ ³) _{3/2} , (d ₊ ⁵) _{5/2}) ₃	21.775(3)	21.8812	2.15(6)
47	Mn	3d ⁷	1	(d ₊ ³) _{9/2}	9	((d ₋ ³) _{3/2} , (d ₊ ⁴) ₄) _{11/2}	17.263(3)	17.2267	1.28(5)
47	Mn	3d ⁷	1	(d ₊ ³) _{9/2}	5	((d ₋ ³) _{3/2} , (d ₊ ⁴) ₄) _{9/2}	19.403(3)	19.4231	1.51(6)
47	Mn	3d ⁷	3	(d ₊ ³) _{5/2}	10	((d ₋ ³) _{3/2} , (d ₊ ⁴) ₂) _{7/2}	20.851(3)	20.8488	1.84(5)
47	Mn	3d ⁷	2	(d ₊ ³) _{3/2}	8	((d ₋ ³) _{3/2} , (d ₊ ⁴) ₂) _{1/2}	21.390(3)	21.4662	1.72(6)
47	Mn	3d ⁷	1	(d ₊ ³) _{9/2}	4	((d ₋ ³) _{3/2} , (d ₊ ⁴) ₄) _{7/2}	21.687(3)	21.7903	2.38(6)
47	Mn	3d ⁷	2	(d ₊ ³) _{3/2}	7	((d ₋ ³) _{3/2} , (d ₊ ⁴) ₄) _{5/2}	21.916(3)	21.9934	6.80(5)
48	Cr	3d ⁶	1	(d ₊ ²) ₄	10	((d ₋ ³) _{3/2} , (d ₊ ³) _{3/2}) ₃	17.300(3)	17.2838	7.07(5)
48	Cr	3d ⁶	1	(d ₊ ²) ₄	8	((d ₋ ³) _{3/2} , (d ₊ ³) _{9/2}) ₅	19.437(3)	19.4248	4.35(5)
48	Cr	3d ⁶	2	(d ₊ ²) ₂	9	((d ₋ ³) _{3/2} , (d ₊ ³) _{3/2}) ₂	19.721(3)	19.7351	1.35(6)
48	Cr	3d ⁶	1	(d ₊ ²) ₄	5	((d ₋ ³) _{3/2} , (d ₊ ³) _{9/2}) ₄	22.091(3)	22.1559	2.00(6)
48	Cr	3d ⁶	1	(d ₊ ²) ₄	4	((d ₋ ³) _{3/2} , (d ₊ ³) _{9/2}) ₃	22.754(3)	22.8747	1.69(6)
49	V	3d ⁵	1	(d ₊) _{5/2}	10	((d ₋ ³) _{3/2} , (d ₊ ²) ₀) _{3/2}	13.487(3)	13.4510	1.82(5)
49	V	3d ⁵	1	(d ₊) _{5/2}	9	((d ₋ ³) _{3/2} , (d ₊ ²) ₂) _{7/2}	16.275(3)	16.2253	8.31(4)
49	V	3d ⁵	1	(d ₊) _{5/2}	5	((d ₋ ³) _{3/2} , (d ₊ ²) ₂) _{3/2}	19.583(3)	19.6141	2.54(6)
49	V	3d ⁵	1	(d ₊) _{5/2}	3	((d ₋ ³) _{3/2} , (d ₊ ²) ₄) _{7/2}	20.114(3) ^b	20.1278	1.05(6)
49	V	3d ⁵	1	(d ₊) _{5/2}	2	((d ₋ ³) _{3/2} , (d ₊ ²) ₄) _{5/2}	24.711(3)	24.8671	2.19(6)
50	Ti	3d ⁴	5	((d ₋ ³) _{3/2} , d ₊) ₃	17	((d ₋ ²) ₀ , (d ₊ ²) ₄) ₄	15.105(3)	15.0733	7.48(5)
50	Ti	3d ⁴	3	((d ₋ ³) _{3/2} , d ₊) ₄	13	((d ₋ ²) ₂ , (d ₊ ²) ₂) ₃	18.043(3)	18.0451	1.19(6)
50	Ti	3d ⁴	2	((d ₋ ³) _{3/2} , d ₊) ₁	7	((d ₋ ²) ₂ , (d ₊ ²) ₄) ₂	19.148(3)	19.1681	3.13(6)
50	Ti	3d ⁴	3	((d ₋ ³) _{3/2} , d ₊) ₄	10	((d ₋ ²) ₂ , (d ₊ ²) ₄) ₅	20.410(3)	20.4503	1.10(6)
50	Ti	3d ⁴	1	(d ₊ ⁴) ₀	2	((d ₋ ³) _{3/2} , d ₊) ₁	22.325(3)	22.4327	2.17(6)
50	Ti	3d ⁴	3	((d ₋ ³) _{3/2} , d ₊) ₄	8	((d ₋ ²) ₂ , (d ₊ ²) ₄) ₄	22.502(3)	22.6346	1.98(6)
51	Sc	3d ³	1	(d ₊ ²) _{3/2}	7	((d ₋ ²) ₀ , d ₊) _{5/2}	13.706(3)	13.6749	1.92(5)
51	Sc	3d ³	5	((d ₋ ²) ₂ , d ₊) _{9/2}	12	(d ₋ , (d ₊ ²) ₄) _{11/2}	17.873(3)	17.8904	9.60(5)
51	Sc	3d ³	1	(d ₊ ³) _{3/2}	6	((d ₋ ²) ₂ , d ₊) _{1/2}	18.150(6)	18.1838	6.84(5)
51	Sc	3d ³	2	((d ₋ ²) ₂ , d ₊) _{5/2}	8	(d ₋ , (d ₊ ²) ₄) _{7/2}	18.942(3)	18.9797	3.29(6)
51	Sc	3d ³	1	(d ₊ ³) _{3/2}	3	((d ₋ ²) ₂ , d ₊) _{3/2}	19.639(3)	19.6876	1.83(6)
51	Sc	3d ³	1	(d ₊ ³) _{3/2}	2	((d ₋ ²) ₂ , d ₊) _{5/2}	21.762(3)	21.8713	2.26(6)
52	Ca	3d ²	1	(d ₊ ²) ₂	5	(d ₋ , d ₊) ₄	16.149(4) [*]	16.1575	2.82(2)
52	Ca	3d ²	1	(d ₊ ²) ₂	4	(d ₋ , d ₊) ₂	16.884(3)	16.9070	1.23(6)
52	Ca	3d ²	1	(d ₊ ²) ₂	3	(d ₋ , d ₊) ₃	19.525(3)	19.6012	2.48(6)
52	Ca	3d ²	2	(d ₊ ²) ₀	6	(d ₋ , d ₊) ₁	22.158(3)	22.2673	1.13(6)
53	K	3p ⁵ 3d ²	6	((p ₊ ³) _{3/2} , (d ₋ ²) ₂) _{7/2}	19	((p ₊ ³) _{3/2} , d ₋ d ₊) _{9/2}	14.576(3)	14.5240	8.75(4)
53	K	3d	1	(d ₋) _{3/2}	2	(d ₊) _{5/2}	18.158(3)	18.2132, 18.1578 ^C	1.76(6)
53	K	3p ⁵ 3d ²	6	((p ₊ ³) _{3/2} , (d ₋ ²) ₂) _{7/2}	9	((p ₊ ³) _{3/2} , d ₋ d ₊) _{9/2}	21.316(3)	21.4145	1.96(6)
54	Ar	3p ⁵ 3d	5	((p ₊ ³) _{3/2} , d ₋) ₂	8	((p ₊ ³) _{3/2} , d ₊) ₃	16.693(3)	16.7008	1.76(6)
54	Ar	3p ⁵ 3d	4	((p ₊ ³) _{3/2} , d ₋) ₃	6	((p ₊ ³) _{3/2} , d ₊) ₄	19.958(3)	20.0564	1.39(6)

Table 4. Identified spectral lines of highly-charged ions of tantalum. Level identifications include calculated level numbers. Blended lines are indicated by “b”. Notation a(b) for transition probabilities A means $a \cdot 10^b$. Other theoretical works: A – [39], B – [40], C – [41].

Ion charge	Seq.	Conf.	Lower level		Upper level		λ_{exp} (nm)	λ_{th} (nm)	A (s^{-1})
			No.	Term _J	No.	Term _J			
45	Ni	$3d^9 4s$	3	$((d_+^5)_{5/2}, s_+)_2$	4	$((d_-^3)_{3/2}, s_+)_1$	20.482(3)	20.5428, 20.4758 ^A	1.96(6)
46	Co	$3d^9$	1	$(d_+^5)_{5/2}$	2	$(d_-^3)_{3/2}$	19.843(3)	19.9229, 19.816(32) ^B	2.02(6)
47	Fe	$3d^8$	1	$(d_+^4)_4$	7	$((d_-^3)_{3/2}, (d_+^5)_{5/2})_4$	16.436(3)	16.4099	8.37(5)
47	Fe	$3d^8$	2	$(d_+^4)_2$	6	$((d_-^3)_{3/2}, (d_+^5)_{5/2})_1$	18.667(3)	18.6907	1.40(6)
47	Fe	$3d^8$	2	$(d_+^4)_2$	5	$((d_-^3)_{3/2}, (d_+^5)_{5/2})_2$	20.204(3)	20.2858	1.59(6)
47	Fe	$3d^8$	1	$(d_+^4)_4$	4	$((d_-^3)_{3/2}, (d_+^5)_{5/2})_3$	20.322(3)	20.4182	2.64(6)
48	Mn	$3d^7$	1	$(d_+^3)_{9/2}$	9	$((d_-^3)_{3/2}, (d_+^4)_4)_{11/2}$	16.281(4)	16.2525	1.56(5)
48	Mn	$3d^7$	5	$((d_-^3)_{3/2}, (d_+^4)_4)_{9/2}$	15	$((d_-^2)_2, (d_+^5)_{5/2})_{9/2}$	17.640(3)	17.6608	1.81(6)
48	Mn	$3d^7$	3	$(d_+^3)_{5/2}$	11	$((d_-^2)_{3/2}, (d_+^4)_2)_{5/2}$	18.169(3)	18.1220	7.02(5)
48	Mn	$3d^7$	1	$(d_+^3)_{9/2}$	5	$((d_-^3)_{3/2}, (d_+^4)_4)_{9/2}$	18.210(3)	18.2328	1.85(6)
48	Mn	$3d^7$	3	$(d_+^3)_{5/2}$	10	$((d_-^3)_{3/2}, (d_+^4)_2)_{7/2}$	19.508(3)	19.5120	2.28(5)
48	Mn	$3d^7$	2	$(d_+^3)_{3/2}$	8	$((d_-^3)_{3/2}, (d_+^4)_2)_{1/2}$	19.968(3)	20.0415	2.11(6)
48	Mn	$3d^7$	1	$(d_+^3)_{9/2}$	4	$((d_-^3)_{3/2}, (d_+^4)_4)_{7/2}$	20.215(3)	20.3167	2.92(6)
48	Mn	$3d^7$	2	$(d_+^3)_{3/2}$	7	$((d_-^2)_{3/2}, (d_+^4)_4)_{5/2}$	20.417(3)	20.4889	8.38(5)
48	Mn	$3d^7$	3	$(d_+^3)_{5/2}$	7	$((d_-^3)_{3/2}, (d_+^4)_4)_{5/2}$	23.031(3)	23.1203	7.00(5)
48	Mn	$3d^7$	3	$(d_+^3)_{5/2}$	6	$((d_-^3)_{3/2}, (d_+^4)_2)_{3/2}$	23.938(3) ^b	24.0887	1.38(6)
49	Cr	$3d^6$	1	$(d_+^2)_4$	15	$((d_-^3)_{3/2}, (d_+^3)_{5/2})_3$	13.462(3)	13.3992	3.39(5)
49	Cr	$3d^6$	1	$(d_+^2)_4$	12	$((d_-^3)_{3/2}, (d_+^3)_{5/2})_4$	13.861(3)	13.8207	3.13(4)
49	Cr	$3d^6$	2	$(d_+^2)_2$	15	$((d_-^2)_{3/2}, (d_+^3)_{5/2})_3$	14.665(3)	14.6071	4.07(5)
49	Cr	$3d^6$	1	$(d_+^2)_4$	10	$((d_-^3)_{3/2}, (d_+^3)_{3/2})_3$	16.286(4)	16.2870	8.47(5)
49	Cr	$3d^6$	1	$(d_+^2)_4$	8	$((d_-^3)_{3/2}, (d_+^3)_{9/2})_5$	18.242(5)	18.2370	5.35(5)
49	Cr	$3d^6$	2	$(d_+^2)_2$	9	$((d_-^3)_{3/2}, (d_+^3)_{3/2})_2$	18.486(3)	18.5076	1.66(6)
49	Cr	$3d^6$	1	$(d_+^2)_4$	5	$((d_-^3)_{3/2}, (d_+^3)_{9/2})_4$	20.602(3)	20.6685	2.46(6)
49	Cr	$3d^6$	1	$(d_+^2)_4$	4	$((d_-^2)_{3/2}, (d_+^3)_{9/2})_3$	21.144(3)	21.2545	2.08(6)
49	Cr	$3d^6$	2	$(d_+^2)_2$	6	$((d_-^3)_{3/2}, (d_+^3)_{3/2})_1$	22.214(3)	22.3583	2.66(6)
50	V	$3d^5$	1	$(d_+)_5/2$	10	$((d_-^3)_{3/2}, (d_+^2)_0)_{3/2}$	12.787(3)	12.7531	2.16(5)
50	V	$3d^5$	1	$(d_+)_5/2$	9	$((d_-^3)_{3/2}, (d_+^2)_2)_{7/2}$	15.374(3)	15.3315	1.00(5)
50	V	$3d^5$	1	$(d_+)_5/2$	5	$((d_-^3)_{3/2}, (d_+^2)_2)_{3/2}$	18.352(3)	18.3840	3.09(6)
50	V	$3d^5$	1	$(d_+)_5/2$	3	$((d_-^2)_{3/2}, (d_+^2)_4)_{7/2}$	18.841(3) ^b	18.8579	1.30(6)
50	V	$3d^5$	4	$((d_-^3)_{3/2}, (d_+^2)_4)_{11/2}$	15	$((d_-^2)_2, (d_+^3)_{9/2})_{13/2}$	18.841(3) ^b	18.8432	4.23(5)
50	V	$3d^5$	4	$((d_-^3)_{3/2}, (d_+^2)_4)_{11/2}$	13	$((d_-^2)_2, (d_+^3)_{9/2})_{11/2}$	20.368(3)	20.4465	1.88(6)
50	V	$3d^5$	1	$(d_+)_5/2$	2	$((d_-^3)_{3/2}, (d_+^2)_4)_{5/2}$	22.869(3)	23.0137	2.73(6)
51	Ti	$3d^4$	5	$((d_-^3)_{3/2}, d_+)_3$	17	$((d_-^2)_0, (d_+^2)_4)_4$	14.303(3)	14.2704	9.03(5)
51	Ti	$3d^4$	3	$((d_-^3)_{3/2}, d_+)_4$	10	$((d_-^2)_2, (d_+^2)_4)_5$	19.073(3)	19.1147	1.35(6)
51	Ti	$3d^4$	1	$(d_+^1)_0$	2	$((d_-^3)_{3/2}, d_+)_1$	20.750(3)	20.8492	2.69(6)
52	Sc	$3d^3$	1	$(d_-^3)_{3/2}$	7	$((d_-^2)_0, d_+)_{5/2}$	12.987(7)	12.9603	2.31(5)
52	Sc	$3d^3$	1	$(d_-^3)_{3/2}$	6	$((d_-^2)_2, d_+)_{1/2}$	17.053(3)	17.0818	8.37(5)
52	Sc	$3d^3$	2	$((d_-^2)_2, d_+)_{5/2}$	8	$(d_-, (d_+^2)_4)_{7/2}$	17.758(3)	17.8065	4.01(6)
52	Sc	$3d^3$	1	$(d_-^2)_{3/2}$	3	$((d_-^2)_2, d_+)_{3/2}$	18.377(3)	18.4346	2.24(6)
52	Sc	$3d^3$	1	$(d_-^2)_{3/2}$	2	$((d_-^2)_2, d_+)_{5/2}$	20.247(3)	20.3630	2.78(6)
53	Ca	$3d^2$	1	$(d_-^2)_2$	4	$(d_-, d_+)_2$	15.885(3)	15.9086	1.49(6)
53	Ca	$3d^2$	1	$(d_-^2)_2$	3	$(d_-, d_+)_3$	18.250(3)	18.3192	3.02(6)
53	Ca	$3d^2$	2	$(d_-^2)_0$	6	$(d_-, d_+)_1$	20.598(3)	20.6941	1.40(6)
54	K	$3d$	1	$(d_-)_{3/2}$	2	$(d_+)_{5/2}$	17.015(3)	17.0662, 17.0145 ^C	2.14(6)
54	K	$3p^5 3d^2$	6	$((p_+^3)_{3/2}, (d_-^2)_2)_{7/2}$	9	$((p_+^3)_{3/2}, d_-, d_+)_{9/2}$	19.831(3)	19.9134	2.43(6)
55	Ar	$3p^5 3d$	5	$((p_+^3)_{3/2}, d_-)_2$	8	$((p_+^3)_{3/2}, d_+)_3$	15.699(3)	15.7090	2.12(6)
55	Ar	$3p^5 3d$	4	$((p_+^3)_{3/2}, d_-)_3$	6	$((p_+^3)_{3/2}, d_+)_4$	18.607(3)	18.6975	1.71(6)
56	Cl	$3p^4 3d$	3	$((p_+^2)_2, d_-)_{5/2}$	7	$((p_+^2)_2, d_+)_{7/2}$	17.735(3)	17.7940	1.51(6)
56	Cl	$3p^4 3d$	5	$((p_+^2)_2, d_-)_{7/2}$	8	$((p_+^2)_2, d_+)_{9/2}$	18.093(3)	18.1197	1.88(6)
57	S	$3p^3 3d$	6	$(p_+, d_-)_3$	7	$(p_+, d_+)_4$	17.561(3)	17.5900	2.14(6)

Table 5. Identified spectral lines of highly-charged ions of gold. Level identifications include calculated level numbers. Blended lines are indicated by “b”. Notation a(b) for transition probabilities A means $a \cdot 10^b$. Electric-quadrupole lines are marked by asterisks. Other theoretical works: A – [39], B – [40], C – [41].

Ion charge	Seq.	Conf.	Lower level		Upper level		λ_{exp} (nm)	λ_{th} (nm)	A (s^{-1})
			No.	Term $_J$	No.	Term $_J$			
51	Ni	$3d^9 4s$	3	$((d_+^5)_{5/2}, s_+)_2$	4	$((d_-^3)_{3/2}, s_+)_1$	13.858(3)	13.8971, 13.8550 ^A	6.23(6)
52	Co	$3d^9$	1	$(d_+^5)_{5/2}$	2	$(d_-^3)_{3/2}$	13.517(3)	13.5678, 13.497(27) ^B	6.38(6)
53	Fe	$3d^8$	1	$(d_+^4)_4$	6	$((d_-^3)_{3/2}, (d_+^5)_{5/2})_4$	11.707(3)	11.6996	2.52(6)
53	Fe	$3d^8$	2	$(d_+^4)_2$	7	$((d_-^3)_{3/2}, (d_+^5)_{5/2})_1$	12.854(3)	12.8748	4.38(6)
53	Fe	$3d^8$	1	$(d_+^4)_4$	4	$((d_-^3)_{3/2}, (d_+^5)_{5/2})_3$	13.739(3)	13.7943	8.38(6)
53	Fe	$3d^8$	3	$(d_+^4)_0$	7	$((d_-^3)_{3/2}, (d_+^5)_{5/2})_1$	16.610(3)	16.6990	1.86(6)
54	Mn	$3d^7$	3	$(d_+^3)_{5/2}$	12	$((d_-^3)_{3/2}, (d_+^4)_0)_{3/2}$	10.541(5)	10.5155	2.49(6)
54	Mn	$3d^7$	1	$(d_+^3)_{9/2}$	10	$((d_-^3)_{3/2}, (d_+^4)_2)_{7/2}$	10.783(3)	10.7761	3.89(5)
54	Mn	$3d^7$	1	$(d_+^3)_{9/2}$	9	$((d_-^3)_{3/2}, (d_+^4)_4)_{11/2}$	11.598(3)	11.5917	4.80(5)
54	Mn	$3d^7$	1	$(d_+^3)_{9/2}$	5	$((d_-^3)_{3/2}, (d_+^4)_4)_{9/2}$	12.650(3) ^b	12.6728	5.70(6)
54	Mn	$3d^7$	1	$(d_+^3)_{9/2}$	4	$((d_-^3)_{3/2}, (d_+^4)_4)_{7/2}$	13.627(3)	13.6811	9.29(6)
55	Cr	$3d^6$	1	$(d_+^2)_4$	15	$((d_-^3)_{3/2}, (d_+^3)_{5/2})_3$	9.910(3)	9.8848	9.56(5)
55	Cr	$3d^6$	1	$(d_+^2)_4$	12	$((d_-^3)_{3/2}, (d_+^3)_{5/2})_4$	10.117(3)	10.0994	8.98(5)
55	Cr	$3d^6$	2	$(d_+^2)_2$	15	$((d_-^3)_{3/2}, (d_+^3)_{5/2})_3$	10.652(3)	10.6295	1.22(6)
55	Cr	$3d^6$	2	$(d_+^2)_2$	14	$((d_-^3)_{3/2}, (d_+^3)_{5/2})_2$	10.764(3)	10.755	7.40(5)
55	Cr	$3d^6$	1	$(d_+^2)_4$	10	$((d_-^3)_{3/2}, (d_+^3)_{3/2})_3$	11.553(3)	11.5501	2.39(6)
55	Cr	$3d^6$	1	$(d_+^2)_4$	8	$((d_-^3)_{3/2}, (d_+^3)_{9/2})_5$	12.667(3)	12.6774	1.73(6)
55	Cr	$3d^6$	2	$(d_+^2)_2$	9	$((d_-^3)_{3/2}, (d_+^3)_{3/2})_2$	12.773(3)	12.7997	5.20(6)
55	Cr	$3d^6$	1	$(d_+^2)_4$	5	$((d_-^3)_{3/2}, (d_+^3)_{9/2})_4$	13.869(3)	13.9155	7.98(6)
55	Cr	$3d^6$	1	$(d_+^2)_4$	4	$((d_-^3)_{3/2}, (d_+^3)_{9/2})_3$	14.025(3)	14.0868	6.85(6)
55	Cr	$3d^6$	2	$(d_+^2)_2$	6	$((d_-^3)_{3/2}, (d_+^3)_{3/2})_1$	14.562(3)	14.6410	8.98(6)
56	V	$3d^5$	1	$(d_+)_{5/2}$	10	$((d_-^3)_{3/2}, (d_+^2)_0)_{3/2}$	9.387(3)	9.3698	5.75(5)
56	V	$3d^5$	1	$(d_+)_{5/2}$	9	$((d_-^3)_{3/2}, (d_+^2)_2)_{7/2}$	11.028(3)	11.0158	2.96(5)
56	V	$3d^5$	1	$(d_+)_{5/2}$	7	$((d_-^3)_{3/2}, (d_+^2)_2)_{5/2}$	11.509(3)	11.5065	9.17(4)
56	V	$3d^5$	1	$(d_+)_{5/2}$	6	$((d_-^3)_{3/2}, (d_+^2)_4)_{9/2}$	11.993(3)*	11.9941	7.97(2)
56	V	$3d^5$	1	$(d_+)_{5/2}$	5	$((d_-^3)_{3/2}, (d_+^2)_2)_{3/2}$	12.647(3) ^b	12.6749	9.52(6)
56	V	$3d^5$	1	$(d_+)_{5/2}$	3	$((d_-^3)_{3/2}, (d_+^2)_4)_{7/2}$	12.947(3)	12.9689	4.22(6)
56	V	$3d^5$	4	$((d_-^3)_{3/2}, (d_+^2)_4)_{11/2}$	13	$((d_-^2)_2, (d_+^3)_{9/2})_{11/2}$	13.652(5)	13.7051	6.11(6)
56	V	$3d^5$	1	$(d_+)_{5/2}$	2	$((d_-^3)_{3/2}, (d_+^2)_4)_{5/2}$	14.862(3)	14.9435	9.34(6)
57	Ti	$3d^4$	3	$((d_-^3)_{3/2}, d_+)_4$	13	$((d_-^2)_2, (d_+^2)_2)_3$	11.870(4)	11.8770	4.39(6)
57	Ti	$3d^4$	3	$((d_-^3)_{3/2}, d_+)_4$	10	$((d_-^2)_2, (d_+^2)_4)_5$	12.991(3)	13.0196	4.30(6)
57	Ti	$3d^4$	1	$(d_+^4)_0$	2	$((d_-^3)_{3/2}, d_+)_1$	13.781(3)	13.8384	8.89(6)
58	Sc	$3d^3$	1	$(d_-^3)_{3/2}$	7	$((d_-^2)_0, d_+)_{5/2}$	9.502(4)	9.4918	6.44(5)
58	Sc	$3d^3$	1	$(d_-^3)_{3/2}$	6	$((d_-^2)_2, d_+)_{1/2}$	11.887(5)	11.9000	2.65(6)
58	Sc	$3d^3$	1	$(d_-^3)_{3/2}$	5	$((d_-^2)_2, d_+)_{7/2}$	12.054(3)*	12.0761	1.55(3)
58	Sc	$3d^3$	1	$(d_-^3)_{3/2}$	3	$((d_-^2)_2, d_+)_{3/2}$	12.590(3)	12.6212	7.14(6)
58	Sc	$3d^3$	1	$(d_-^3)_{3/2}$	2	$((d_-^2)_2, d_+)_{5/2}$	13.501(3)	13.5597	8.98(6)
59	Ca	$3d^2$	1	$(d_-^2)_2$	4	$(d_-, d_+)_2$	11.189(3)	11.2089	4.49(6)
59	Ca	$3d^2$	1	$(d_-^2)_2$	3	$(d_-, d_+)_3$	12.444(3)	12.4874	9.35(6)
59	Ca	$3d^2$	2	$(d_-^2)_0$	6	$(d_-, d_+)_1$	13.656(3)	13.7184	4.65(6)
60	K	$3d$	1	$(d_-)_{3/2}$	2	$(d_+)_{5/2}$	11.750(8) ^b	11.7861, 11.7510 ^C	6.49(6)
60	K	$3p^5 3d^2$	6	$((p_+^3)_{3/2}, (d_-^2)_2)_{7/2}$	9	$((p_+^3)_{3/2}, d_-)_{9/2}$	13.200(3)	13.2556	7.95(6)